

# Supporting Information

Alessandri et al. 10.1073/pnas.1309482110

## SI Materials and Methods

**Coextrusion Device Fabrication.** The central unit of microfluidic devices consists of three axially coaligned glass capillary tubes. The outermost tapered capillary is obtained by pulling a round cross-section capillary [600- $\mu\text{m}$  inner diameter (i.d.), 840- $\mu\text{m}$  outer diameter (o.d.); Vitrocom] with a micropipette puller (P2000; Sutter Instrument). The innermost (100- $\mu\text{m}$  i.d., 170- $\mu\text{m}$  o.d.) and intermediate (300- $\mu\text{m}$  i.d., 400- $\mu\text{m}$  o.d.) capillaries were kept cylindrical and cut at desired lengths. The capillary ends were polished with microabrasive films (1- $\mu\text{m}$  grain; 3M) to avoid any bevel that generates flow perturbation and to reach the desired tip diameter (typically between 130 and 180  $\mu\text{m}$ ). Hydrophobic coating (1H,1H,2H,2H-Perfluorooctyltrimethoxysilane; ABCR) was applied to the capillary walls following standard protocols (1) to prevent any wetting of the outer walls of the injector tip by the alginate solution (AL). Assembly of the coextrusion device was performed under a binocular microscope. The outermost capillary was first glued to a glass slide, which serves as a support to the device. The other two cylindrical capillaries were then inserted and sealed sequentially using an epoxy resin (Loctite 3430; Radisopares-RS Components). Coaxial and longitudinal alignments were manually controlled as the resin cures at room temperature (RT). The inlet ports of the chip were made by gluing the fittings of blunt-tipped syringe needles (NN-1950R; Terumo) on top of the free ends of the capillaries.

**Coextrusion Device Operation.** The three fluid phases [cell suspension (CS), intermediate solution (IS), and AL; Fig. 1] were loaded into syringes (10MDR-LL-GT SGE; Analytical Science) with needles fitted to Teflon tubings (0.5-mm i.d.; Bohlender). The other ends of the tubings were inserted into the appropriate inlets of the coextrusion device, which is clamped vertically to a post inside a laminar flow hood. The syringes were mounted on syringe pumps (PHD 4400; Harvard Apparatus) that control fluid injection at the desired flow rates. In this work, we mostly used two sets of flow rates: (i) for thin capsules:  $q_{CS} = 50 \text{ mL}\cdot\text{h}^{-1}$ ,  $q_{IS} = 50 \text{ mL}\cdot\text{h}^{-1}$ , and  $q_{AL} = 40 \text{ mL}\cdot\text{h}^{-1}$  and (ii) for thick capsules:  $q_{CS} = 20 \text{ mL}\cdot\text{h}^{-1}$ ,  $q_{IS} = 20 \text{ mL}\cdot\text{h}^{-1}$ , and  $q_{AL} = 30 \text{ mL}\cdot\text{h}^{-1}$ . After initiation of the flows, the compound microdroplets are directed to a gelation bath containing 100 mM calcium chloride (VWR International) and traces of Tween 20 surfactant (Merck), and they are placed at approximately at 0.5 m below the outlet of the device. Operation for seconds was sufficient to produce several  $10^4$  capsules, which were immediately washed in isotonic sorbitol solution and transferred to the appropriate culture medium within less than 5 min. After use, the microfluidic device was cleaned with disinfectant (Biocidal ZF; Biovalley), ethanol, and deionized water. Before next use, the chip was rinsed with sorbitol solution.

**AL and CS Preparation.** The outermost phase (AL) was prepared by dissolving 2.5% wt/vol sodium alginate (Protanal LF200S; FMC) in water and by adding 0.5 mM SDS surfactant (VWR International). The solution was filtered at 1  $\mu\text{m}$  (Pall Life Science) and stored at 4  $^{\circ}\text{C}$ .

The intermediate phase (IS) was generally a 300-mM sorbitol (Merck) solution.

The innermost phase (CS) was obtained by detaching cells from the walls of the culture flask with 0.5% Trypsin-EDTA (Invitrogen). After washing in the appropriate culture medium and gentle centrifugation ( $300 \times g$ , 5 min, 20  $^{\circ}\text{C}$ ), the cells were resuspended in 300 mM sorbitol solution at an approximate concentration of  $3 \times 10^6$  cells per milliliter.

**Cell Lines, Monolayer and Encapsulated Cell Cultures.** We used WT mouse colon carcinoma CT26 cells (ATCC CRL-2638; American Tissue Culture Collection) and CT26 cells stably transfected with LifeAct-mCherry (plasmid provided by R. Gaudin; Institut Curie, Unit 932, Paris, France). Tests were also carried out with HeLa cells and mouse sarcoma cells (S180, courtesy of Chu Yeh-Shiu, Institute of Cell and Molecular Biology, Singapore).

All cells were maintained in DMEM (Invitrogen) supplemented with 10% (vol/vol) FBS (Invitrogen) and antibiotics (100  $\mu\text{g}\cdot\text{mL}^{-1}$  streptomycin and 100  $\text{U}\cdot\text{mL}^{-1}$  penicillin; Gibco BRL) in a humidified atmosphere containing 5%  $\text{CO}_2$  at 37  $^{\circ}\text{C}$ , with medium changed every 2 d. Cells were grown as subconfluent monolayers to prepare the CSs used for encapsulation in alginate hollow spheres.

Once cellular capsules were formed following the protocol described above, they were placed inside an incubator (37  $^{\circ}\text{C}$ , 5%  $\text{CO}_2$ ,  $\sim 100\%$  relative humidity). Among the thousands of collected cellular capsules, the majority were kept in a Petri dish containing culture medium and cultured in the same conditions as cell monolayers. In each encapsulation run, several tens of capsules were selected for high-resolution imaging. Depending on the microscope configuration requirements and the desired duration of the imaging session (from hours to weeks), these selected cellular capsules were transferred to dedicated culture chambers or devices (see description below).

For comparison with our method, CT26 spheroids were also grown according to the classical agarose cushion technique (2).

**Cryosections and Immunofluorescence Staining of Spheroids.** Spheroids were fixed in 4% paraformaldehyde in PBS for 1 h at RT. Following overnight incubation in 30% glucose solution, they were then embedded in optimal cutting temperature (OCT) compound (VWR) and frozen at  $-80^{\circ}\text{C}$ . Slices of 8  $\mu\text{m}$  were cut from OCT-embedded spheroids. OCT was removed by PBS washing. Slices were then incubated for 45 min at RT in PBS complemented with 3% FCS and stored overnight at 4  $^{\circ}\text{C}$  with primary antibody diluted in the same buffer. Secondary fluorescent antibodies and DAPI were added for 45 min. Slices were assembled into mounting medium (Immu-mount; ThermoScientific) after several washes. Specifically, we used KI-67 (AbCys), vimentin (Cell Signaling), collagen I (Abcam), fibronectin (Sigma), and laminin (Sigma). Alexa Fluor-conjugated secondary antibodies and DAPI were purchased from Invitrogen. For in toto cortical actin staining (Fig. 5B), spheroids were incubated with 0.5  $\mu\text{g}\cdot\text{mL}^{-1}$  phalloidin conjugated with Alexa488 (Molecular Probes) in PBS solution with 1% vol/vol Triton-X100 (Sigma) at 4  $^{\circ}\text{C}$  from 2 h to overnight.

**Cell Viability Assessment and Cell Counting.** To assess the efficiency of encapsulation and the cell seeding concentration, phase-contrast images of capsules were taken immediately after encapsulation and the number of cells per capsule was estimated using standard ImageJ (National Institutes of Health) plug-ins (3).

Cell viability was characterized at different stages of encapsulated cell culture with live/dead acetoxymethyl ester of calcein (calcein AM)/ethidium homodimer-1 (EthD-1) dyes (Invitrogen). First, to assess the potential harmfulness of the encapsulation process on suspended cells, we compared the survival rate of cells in suspension (after trypsinization) and inside the capsules (after coextrusion) (Fig. S2). Cells or cellular capsules were incubated with 4  $\mu\text{M}$  EthD-1 and 2.5  $\mu\text{M}$  calcein AM for 5 min. The number of viable cells was determined by counting red (dead) and green (live) cells using an inverted epifluorescence microscope (Axiovert-200M; Carl Zeiss) equipped with an Hg lamp and

an EM CCD camera (C 9100-02; Hamamatsu Photonics). Because encapsulation involves shear of the CS through the submillimetric nozzle and stay in a calcium bath, we performed two complementary experiments to identify the potential origin of survival decrease: (i) CS was injected into the microfluidic device without alginate, and the collection bath was composed of culture medium, or (ii) cells were directly incubated for 5 min to 1 h in a calcium bath. When spheroids were formed and grew within the capsules, the same protocol was adapted by increasing the dye concentrations 10-fold and incubation times to 2–4 h. Equatorial planes of the spheroids were then imaged using confocal microscopy. Although red (dead) cells could be detected in the core of the spheroid, live cells were almost unstained beyond a peripheral rim of a few layers (Fig. S9). This faint internal labeling was due to the fact that the ubiquitous intracellular esterase activity of peripheral cells was sufficient to esterify all cell-permeant calcein AM molecules before they could penetrate deeper into the spheroid.

**Imaging of Long-Term Spheroid Growth, Capsule Deformation, and Collagen Matrix Invasion.** Shell deformation and MCS growth inside capsules or in a collagen matrix were monitored by phase-contrast microscopy.

For all encapsulation runs, 24 capsules were selected from the whole batch of cellular capsules and individually transferred to each well of a multiwell culture plate (Falcon). Each capsule was imaged every 3 h with a Nikon EZ inverted microscope (10×/0.25-N.A. or 20×/0.4-N.A. dry objective) equipped with a color CCD camera (Digital sight DS Fi1; Nikon Instruments) driven by NIS Element software (Nikon Instruments). Image capture was performed at RT and took ~5 min. Between each acquisition, the 24-well plate containing the capsules was kept in the incubator. The culture medium was renewed by one-half every 2 d.

For acquisition of time-lapse sequences with higher temporal resolution (one frame every 5 min) over extended periods of times (~15 d), we also used an inverted microscope (Nikon Eclipse Ti, 10×/0.3-N.A. dry objective; Nikon Instruments) equipped with a motorized stage (Märzhäuser) and climate control system (The Brick; Life Imaging Systems). The microscope and camera (CoolSNAP HQ<sup>2</sup>; Photometrics) were driven by Metamorph software (Molecular Devices). To prevent displacement or drift of the capsules inside the well out of the field of view, we designed a custom-made observation chamber (Fig. S8). Phytigel (Sigma) funnel-like wells were prepared using conical polydimethyl siloxane elastomer (Sylgard-184; Dow Corning) molds fitted to the wells of a 24-well glass-bottom plate. This configuration facilitated loading with individual capsules, which were directed toward the center of the well. The holes (500 μm in diameter) in the phytigel replica, which primarily served as a microconduit, were also found to be efficient in limiting the motions of encapsulated spheroids while inducing no constraint that could alter MCS growth.

For the 3D motility assays, we selected encapsulated spheroids at time  $t = 48$  h after confluence. Alginate shells were dissolved by PBS washing. Bare aggregates were then immersed into a droplet of 2 mg/mL collagen I (BD Biosciences) solution in PBS (pH 7.4) at RT. To avoid contact of the spheroid with the bottom of the glass chamber by sedimentation, the dish was regularly turned upside down until the liquid matrix gelled in situ around the spheroid. Culture medium was then gently added to allow spheroid growth. The embedding protocol was identical for free spheroids.

**Imaging of 3D Cellular Organization of Encapsulated Spheroids.** To visualize the peripheral cell layers and the core of growing spheroids at subcellular resolution, we used monophoton and multiphoton fluorescence confocal microscopy.

Live confocal imaging was performed using an inverted (LSM710; Carl Zeiss) microscope equipped with a climate chamber (Pecon) controlling the CO<sub>2</sub> percentage, temperature, and humidity. The samples were prepared by immersing the capsules in

0.3% low-melting-point agarose (Invitrogen) solution (serum-free culture medium, 37 °C) in a home-made glass-bottom Petri dish (well diameter of ~2 mm). After gelation of agarose pellets (10 min, RT) the Petri dish was filled with culture medium. This mounting allowed immobilization of the capsules, which is required for z-stack acquisition. The percentage of agarose was chosen to generate minimal stress on the growing multicellular spheroids (MCSs). Comparison of growth kinetics between freely moving MCSs and MCSs embedded in agarose revealed no significant difference. To monitor cell dynamics within the spheroid, we used the CT26 LifeAct-mCherry stable line or WT CT26 cells incubated in FM4-64 (2 μg·mL<sup>-1</sup>; Invitrogen). Fluorescence was acquired using a 561-nm (15-mW) diode pumped solid-state laser and a 25×/0.80-N.A. oil immersion objective. The surface of fixed spheroids stained with phalloidin-Alexa488 was imaged with a 488-nm (25-mW) argon laser and a 63×/1.4-N.A. oil immersion objective. Individual images and stacks were processed using Zen 2011 software (Carl Zeiss) and ImageJ. Online movies were edited using After Effects (Adobe) and compressed using Media Encoder (Adobe).

Multiphoton microscopy was performed to access the core of encapsulated spheroids. Two types of microscopes were used: (i) an upright, two-photon, laser-scanning microscope (Lavision) equipped with a 20×/0.95-N.A. water dipping objective (Olympus) and (ii) an inverted LSM710 NLO microscope (Carl Zeiss) equipped with a 25×/0.80-N.A. oil immersion or 40×/1-N.A. water immersion objective (Carl Zeiss). Setups were coupled to femtosecond lasers (690–1,020 nm; Coherent or Spectra Physics). Images of the interior of fixed spheroids stained with phalloidin-Alexa488 were taken at a laser wavelength of 920 nm. Sulforhodamine B (SRB; Sigma) was added to the medium at the concentration of 40 μg·mL<sup>-1</sup>. The best conditions for live imaging of spheroids in culture medium supplemented with SRB were obtained for excitation at 800 nm (4). The capsules were mounted as described for monophoton confocal live imaging.

**Capsule Morphometric Measurements.** Characterization of capsule sizes and shapes was determined on both cell-containing and empty capsules. Measurements on empty capsules, which were obtained by replacing the CS phase with iso-osmotic sorbitol solution, were performed both immediately after encapsulation and after a 1-wk stay in culture medium at 37 °C (to account for potential aging-induced morphological changes). No significant difference was observed between these various conditions. Images of large fields of view of densely packed capsules were taken by phase-contrast microscopy and analyzed using ImageJ. The average capsule radius was defined as  $R = \sqrt{S/\pi}$ , where  $S$  is the equatorial cross-section area of the capsule. The capsule roundness was measured as the ratio of the minor axis to the major axis of the ellipse fitted to the outer edge of the projected equatorial section (Fig. S1). Note that, depending on their orientation, capsules display a small tail, which is inherent to the impact into the gelling bath (e.g., Fig. 2C). However, this slight anisotropy has a negligible effect on the mechanical measurements reported in the main text.

When spheroids have reached confluence, the outer and inner walls of the capsule could be easily detected due to high optical contrast. However, for empty or partially filled capsules, the inner wall of the capsule was weakly visible by phase-contrast microscopy. Capsule thickness measurements were thus performed by doping the AL with 250 μg/mL high-molecular-weight FITC-dextran (2 MDa; Sigma). Capsules images were acquired by confocal microscopy and analyzed with ImageJ. The influence of flow rates on the aspect ratio  $h/R_{out}$  was assessed by comparing experimental data with the theoretical value calculated from volume conservation:  $\frac{h}{R_{out}} = 1 - \left( \frac{q_{in}/q_{out}}{1+q_{in}/q_{out}} \right)^{1/3}$ .

**Alginate Gel Elasticity Measurements.** Although it has been extensively studied, the rheology of alginate gels is still debated (5–7).

In addition to discrepancies between works that use distinct techniques (8, 9), the Young's modulus  $E$  of alginate gels depends on numerous parameters (alginate concentration, chemical composition, and nature and concentration of cross-linking cations) (10). We thus directly probed the bulk gel elasticity of the capsules using three different methods. All measurements were carried out after immersing alginate gels in culture medium for 2 d at 37 °C, which corresponds to the actual experimental conditions.

We first performed atomic force microscopy (AFM) online movies that were edited using After Effects and compressed using Media Encoder microindentation measurements on empty capsules.

Alginate capsules lying on the bottom of a Petri dish filled with culture medium were placed on the sample stage of a Catalyst AFM system (Bruker) mounted on an inverted optical microscope (IX71; Olympus) in force mode (Fig. S6). We used TR400 cantilevers with attached SiO<sub>2</sub> spherical beads (5- $\mu$ m diameter) and of nominal spring constant  $k_{cantilever} = 0.06$  N/m (Novascan). Photodiode sensitivity was calibrated before and after measurements on a freshly cleaved mica surface in PBS. The spring constant was determined using the thermal fluctuations method implemented in Bruker Nanoscope 7.2 software. Force-distance ( $F$ - $z$ ) curves were recorded for displacements of  $\sim 2$   $\mu$ m peak-to-peak amplitude at 0.25–1 Hz. The relative deflection threshold was controlled to reach a capsule deformation between 200 and 500 nm. Data were analyzed in the framework of point load indentation into shallow spheres. The functional force ( $F$ ) – deformation ( $\delta$ ) relationship reads:  $F = \frac{4}{3\sqrt{1-\nu^2}} E \frac{h^2}{R} \delta$  (11). The deformation was calculated in terms of point of contact ( $z_c$ ), actual cantilever position ( $z$ ), deflection offset ( $d_0$ ), and measured deflection ( $d$ ) as  $\delta = z - z_c - (d - d_0)$  (12). Experimentally, the Young's modulus of the alginate gel was derived from the fit of the force-deformation traces (Fig. S6) by taking the measured values for the geometric ( $R$  and  $h$ ) properties of the capsule and  $\nu = 0.5$  for the Poisson ratio. We found  $E = 55 \pm 44$  kPa ( $\pm$ SD,  $n = 7$ ).

The second method consisted of performing traction measurements on macroscopic spaghetti-like cylinders of alginate gel. These threads (length,  $L_0 \sim 0.2$  m; diameter,  $D_0 \sim 1$  mm) were formed with a simple one-way extrusion device with a nozzle size of  $\sim 1$  mm by immersing the tip in the calcium bath to suppress the capillarity instability. Controlled stress  $\sigma$  was applied with a series of calibrated weights  $m$  hooked to alginate cylinders. The elongation  $\Delta L/L_0$  of the alginate sample was measured with a ruler. Assuming  $\nu = 0.5$ , the Young's modulus was derived from  $\sigma = \frac{4mg}{\pi D_0^2(1-\Delta L/L_0)} = E \cdot \frac{\Delta L}{L_0}$ . We found  $E = 71 \pm 12$  kPa ( $\pm$ SD,  $n = 9$ ).

A third determination of  $E$  was based on an osmotic swelling assay. To do so, we replaced the CS with a solution of sorbitol with 5% (wt/vol) dextran (molecular mass = 2 MDa and 500 kDa; Sigma Biochemika). The calcium bath solution and the storage culture medium were also supplemented with 5% (wt/vol) dextran. All solutions were checked to confirm that they were iso-osmotically balanced. To achieve detectable swelling, very thin-walled capsules were prepared ( $q_{in}/q_{out} = 10$ , corresponding to shell thickness  $h \sim 5$ –7  $\mu$ m). Stepwise dilution of dextran caused osmotic swelling of capsules. Concentration differences in dextran were converted into osmotic pressures  $\Pi_0$ , and capsule dilation  $\Delta R/R_0$  was directly measured. At first order, in the limit of small deformation, the alginate Young's modulus was derived by balancing the elastic energy of the spherical shell and the work done by the osmotic pressure difference:  $E \approx \frac{1}{4h_0/R_0} \cdot \left(\frac{\Delta R/R_0}{\pi_0}\right)^{-1}$  (a detailed calculation is provided in *SI Discussion and Equations*). Also, note that no hysteresis was observed in osmotic swelling/shrinking cycles and no temporal evolution of deformation was detected when osmotic pressure difference was maintained for longer periods of time, suggesting that the hydrogel behaves as a purely elastic material for strain less than about 15%.

**Analysis of Spheroid Growth and Capsule Deformation.** The time-lapse, phase-contrast images were analyzed using a custom-made, gradient-based edge detection algorithm implemented in MATLAB (MathWorks). Starting from the center of the capsule, intensity profiles were taken radially and inspected for peaks in the first derivative to extract the contour of the MCS, and the enclosing capsule in each frame was recorded.  $R_{out}$  was derived from the projected cross-sectional area. A similar approach was pursued to monitor the radius of the multicellular spheroid,  $R_{MCS}$ , inside the capsule. The detected noise before confluence was mostly due to rotational movements of the nonperfectly spherical cellular aggregate. The confluence time ( $t = 0$ ) was determined as the time for which MCS growth exhibits an inflection point. We checked that this time coincides with less than 5 min with the visual determination of confluence (on movies with high temporal resolution). Pre- and postconfluent stages were also quantified by a roughness parameter,  $\rho = P/2\sqrt{\pi A}$ , with  $P$  and  $A$  being, respectively, the perimeter and the area of an equatorial cross-section. Although the time evolution of  $\rho$  is noisy in the early stages of MCS growth, it decreases as the spheroid comes closer to the capsule wall before it saturates at a minimal value close to the theoretical value of 1 for perfectly spherical objects.

## SI Discussion and Equations

**Determination of the Young's Modulus of Alginate Gel from Capsule Osmotic Swelling.** We consider a spherical capsule made of an alginate shell enclosing a solution of high-molecular-weight dextran (molecular mass = 500 kDa or 2 MDa) immersed in a less concentrated solution of dextran. Because the shell is permeable to water but not to dextran (Stokes radii of  $\sim 15$  nm and 27 nm), water molecules diffuse into the capsule, which swells until the elastic force of the stretched capsule balances the osmotic pressure (Fig. S6A).

At the onset of the assay, the concentrations of dextran inside and outside the capsule are equal. The initial capsule radius is  $R_0$ . Then, the concentration of dextran in the external bath is decreased by dilution, so that the concentration difference is  $c_0$ . Upon swelling, the capsule radius increases by  $\Delta R = R - R_0$ , and the concentration difference decreases from  $c_0$  to  $c$ :

$$c = c_0 \cdot \left(\frac{R_0}{R}\right)^3. \quad [S1]$$

The stretching elastic energy is given by the following (13):

$$G_{el} = 4\pi \frac{E}{1-\nu} h (R - R_0)^2, \quad [S2]$$

where  $h$  is the shell thickness and  $\nu$  is the Poisson's ratio. For an incompressible material,  $\nu = 1/2$  and the shell becomes thinner as the capsule swells according to:

$$h = h_0 \cdot \left(\frac{R_0}{R}\right)^2, \quad [S3]$$

with  $h_0$  being the thickness of the unstretched capsule.

Because the solutes are very large, the osmotic pressure  $\Pi$  deviates significantly from the nominal value ( $\Pi = nk_B T$ , where  $n$  is the number of osmotically active species and  $k_B T$  is the thermal energy) and is found to be independent of their nominal osmolality beyond a given threshold (molecular mass = 200 kDa for dextran) (14). Different empirical expressions are reported to fit osmotic pressure data (15, 16). For the sake of simplicity, we take the well-established polynomial expression for  $\Pi$  as a function of  $c$  (in wt/vol percentage) (15):

$$\Pi = \alpha c + \beta c^2 + \gamma c^3, \quad [\text{S4}]$$

with  $\alpha = 286$ ,  $\beta = 87$ , and  $\gamma = 5$ . The work done by the osmotic pressure to swell the capsule from  $R_0$  to  $R$  is given by:

$$W = \int_{R_0}^R \Pi \cdot 4\pi R^2 dR. \quad [\text{S5}]$$

Taking into account the dilution effect (Eq. S1), we get:

$$W = 4\pi R_0^3 \left( \alpha c_0 \ln \left( \frac{R}{R_0} \right) + \frac{1}{3} \beta c_0^2 \left( 1 - \left( \frac{R_0}{R} \right)^3 \right) + \frac{1}{6} \gamma c_0^3 \left( 1 - \left( \frac{R_0}{R} \right)^6 \right) \right). \quad [\text{S6}]$$

The equilibrium capsule radius is given by the minimum of the total energy:  $G_{el} + W$ . By further assuming small deformations,  $\Delta R/R_0 \ll 1$ , we arrive at:

$$\frac{\Delta R}{R_0} = \frac{\Pi_0}{\Pi_c + 4E(h_0/R_0)}, \quad [\text{S7}]$$

with  $\Pi_0$  being the osmotic pressure at  $c_0$  and  $\Pi_c = \Pi_0 + 3\beta c_0^2 + 6\gamma c_0^3$ . This reveals that the osmotic pressure  $\Pi_0$  varies from 0 to 4 kPa within the explored range of concentration differences. The approximation given in *Materials and Methods* relies on the assumption that the correction introduced by  $\Pi_c$  remains negligible with respect to the effective Young's modulus  $E \times 4h_0/R_0$ . Taking  $E = 68$  kPa and  $h_0/R_0 \sim 0.05$ , this only holds for  $c_0 < 2\%$ . Under our experimental conditions ( $c_0$  varying from 0 to almost 5%), a more accurate determination of  $E$  (Fig. S6B) requires the use of Eq. S7.

**Phenomenological Approach for Nonlinear Elasticity of Alginate Capsules at Large Deformations.** To confirm the measurement for the Young's modulus derived from the osmotic swelling assay, we developed another mechanical assay, which consisted of directly assessing the stress ( $\sigma$ )–strain ( $\varepsilon$ ) relation of alginate gel threads (Fig. S6D). These threads (1 mm in diameter) were stretched with calibrated weights welded with tiny alginate droplets to one end. In the small deformation regime (typically for relative elongation,  $\varepsilon = \Delta L/L_0 < 10\%$ ), the stress–strain response is linear and the derived Young's modulus is in good agreement with the one previously measured ( $E = 71 \pm 12$  kPa). At very large elongation ( $>80\%$ ), water was observed to pearl out of the sample and significant plasticity was apparent. For intermediate deformation, the material displayed a nonlinear stress–strain response (Fig. S2). Such a strain-hardening behavior is very common for biopolymer gels and has already been reported for alginate gels (17). Because the thin capsules ( $h/R \sim 0.1$ ) that have been extensively used in this work exhibit maximal radial deformation  $\Delta R/R_0 \sim 30\%$  before bursting, accurate determination of the pressure exerted by the expanding confined spheroid is required to take this effect into account. A classical phenomenological approach for nonlinear elasticity consists of considering a corrective term in  $\varepsilon^2$  for the stress ( $\sigma = E\varepsilon + A\varepsilon^2$ ). Instead, by fitting the  $\sigma - \varepsilon$  data with a second-order polynomial expression, we defined an effective strain-dependent elastic modulus  $E_{eff}(\varepsilon) = E(1 + a\varepsilon)$  and found  $a = 1.5$ . We used this expression for  $E$  to derive the pressure from the deformation data on thin capsules.

**Dilation of a Thick-Walled, Internally Pressurized Spherical Vessel.** We assume that the alginate gel is isotropic and that strains are small

(i.e.,  $<10\%$ ). However, if the condition  $h/R \ll 1$  is not fulfilled, the assumption of constant tangential stress across the thickness of the vessel does not hold. In the general case of Poisson's ratio  $\nu \neq 1/2$ , we shall recall the expressions for the radial and hoop stresses (18):

$$\sigma_r = \frac{PR_{in}^3}{R_{out}^3 - R_{in}^3} \left( 1 - \frac{R_{out}^3}{R^3} \right), \quad [\text{S8}]$$

$$\sigma_\varphi = \frac{PR_{in}^3}{2(R_{out}^3 - R_{in}^3)} \left( 2 + \frac{R_{out}^3}{R^3} \right), \quad [\text{S9}]$$

with  $R_{in} \leq R \leq R_{out}$ .

The radial displacement  $u(R)$  is obtained from Hook's law:

$$u(R) = \frac{(1-\nu)\sigma_r - \nu\sigma_\varphi}{E} R. \quad [\text{S10}]$$

Collecting these results, we arrive at:

$$u(R) = \frac{P}{E} \frac{R_{in}^3}{R_{out}^3 - R_{in}^3} \left[ (1-2\nu)R + \frac{(1+\nu)R_{out}^3}{2R^2} \right]. \quad [\text{S11}]$$

If the material is incompressible, we may simplify this equation and write it for two particular cases of interest, namely,  $R = R_{in}$  and  $R = R_{out}$ :

$$u(R_{in}) = \frac{3P}{4E} \frac{R_{in}}{1 - (R_{in}/R_{out})^3}, \quad [\text{S12}]$$

$$u(R_{out}) = \frac{3P}{4E} \frac{R_{out}}{(R_{out}/R_{in})^3 - 1}. \quad [\text{S13}]$$

Finally, from volume conservation of the shell, we have:

$$R_{out}^3(t) - R_{in}^3(t) = R_{out}^3(0) - R_{in}^3(0) = \Delta(R_0^3). \quad [\text{S14}]$$

Using this equation, we separate the time variables  $R_{in}(t)$  and  $R_{out}(t)$  and write the pressure  $P(t)$  as a function of either  $R_{in}(t)$  or  $R_{out}(t)$ . Experimentally, we thus need to measure only the initial outer and inner radii and track the evolution of either the inner or outer radius of the capsule:

$$P(t) = \frac{4}{3}E \left[ 1 - \frac{1}{1 + \Delta(R_0^3)/R_{in}^3(t)} \right] \frac{u(R_{in}(t))}{R_{in}(t)}, \quad [\text{S14}]$$

$$P(t) = \frac{4}{3}E \left[ \frac{1}{1 - \Delta(R_0^3)/R_{out}^3(t)} - 1 \right] \frac{u(R_{out}(t))}{R_{out}(t)}. \quad [\text{S15}]$$

Note that, returning to the general case described by Eq. S11 and constructing the ratio of the displacements at the inner and outer surfaces, we find (19):

$$\frac{u(R_{out})}{u(R_{in})} = \frac{3(1-\nu)\rho}{2(1-2\nu) + (1+\nu)\rho^3}, \quad [\text{S16}]$$

with  $\rho = R_{out}/R_{in} > 1$ .

First, because this ratio is always less than unity, the displacement at the outer radius is smaller than that at the inner radius, which is intuitive and experimentally observed. Second,  $u(R_{out})/u(R_{in})$  provides a direct estimate of the Poisson's ratio, which was found to be  $\nu = 1/2$ .





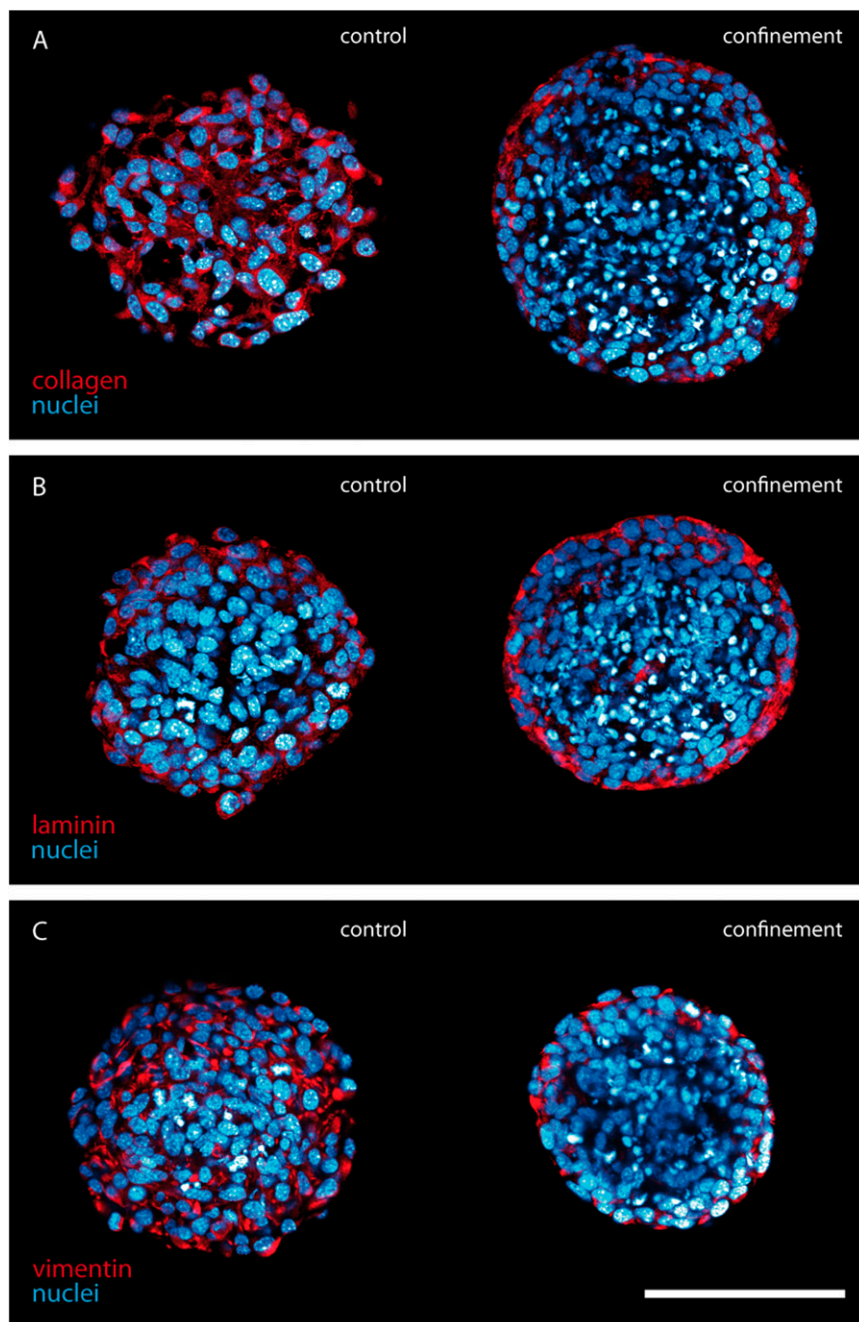


**Fig. S5.** Immunofluorescence staining. Confocal images of free and confined spheroids after cryosection and immunolabeling for DAPI (blue), collagen (A; red), laminin (B; red) and vimentin (C; red) are shown. (Scale bar: 200  $\mu\text{m}$ .)



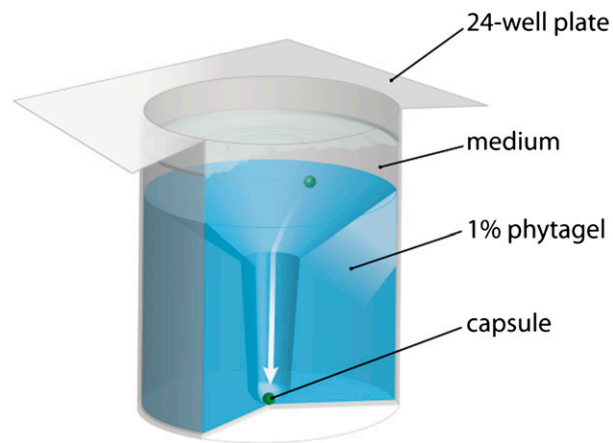


**Fig. 58.** Design of the custom-made observation chamber for long-term imaging of individual cellular capsules. Wells of a multiwell culture plate are filled with phytigel plugs. The funnel shape guides the positioning of single capsules. The tubular hole restricts undesired displacements of the capsule during image acquisition while generating no mechanical stress. Phytigel plugs are replicas of polydimethyl siloxane elastomer (PDMS) molds.

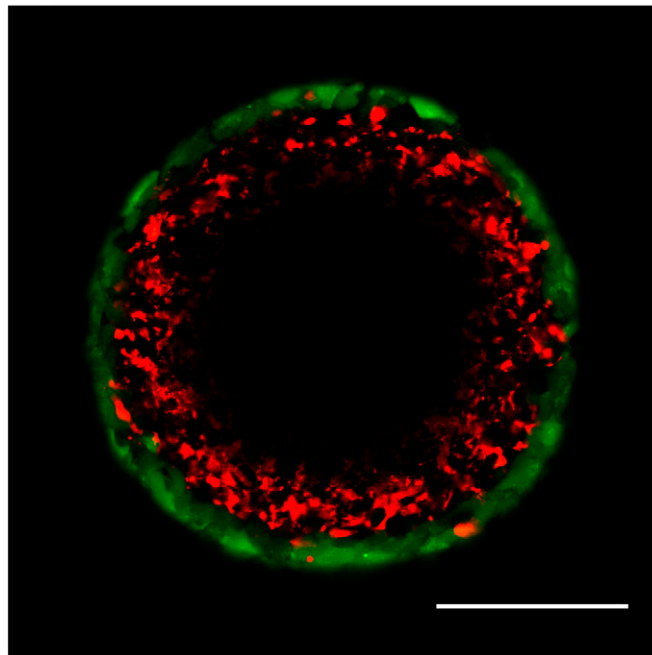
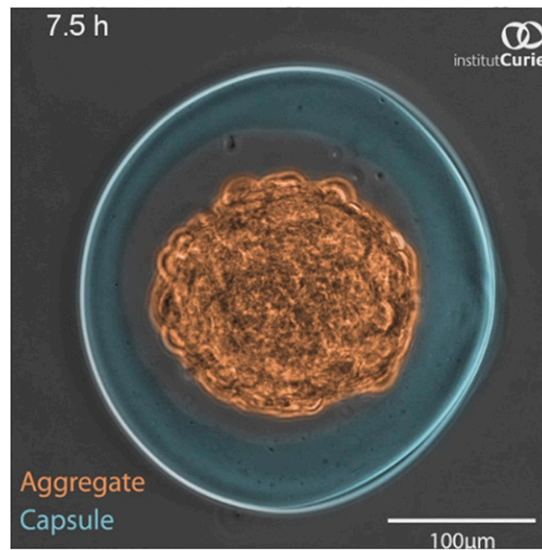


**Fig. 59.** Imaging of cell viability in a postconfluent encapsulated spheroid. Monophoton confocal section of a CT26 spheroid labeled with live/dead dyes is shown. The core of the spheroid is unstained due to insufficient depth of penetration of light and restricted diffusion of the dyes. Dead (red) cells are mostly detected beyond a thin rim of living (green) cells. Calcein (marker for live cells) is accumulated within the peripheral cellular layers. (Scale bar: 100  $\mu\text{m}$ .)



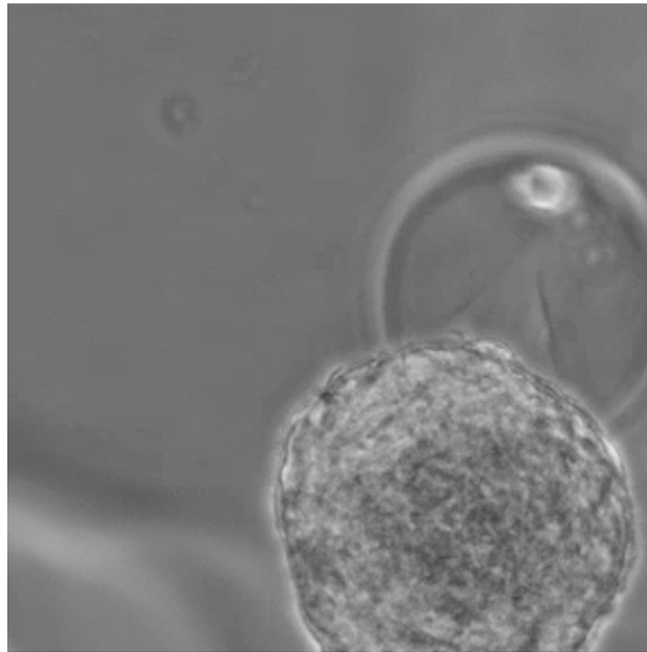
**Movie S1.** Capillary instability. Shown are images acquired at 6,000 frames per second of the compound liquid (AL surrounding CS) exiting the coextrusion device in the different working modes corresponding to different flow rates: (i) dripping ( $55 \text{ mL}\cdot\text{h}^{-1}$ ), (ii) jet breakup into droplets due to the capillary instability ( $100 \text{ mL}\cdot\text{h}^{-1}$ ), and (iii) jetting with intact length larger than the distance between the nozzle and calcium bath ( $300 \text{ mL}\cdot\text{h}^{-1}$ ). (Scale bar: 0.5 mm.)

[Movie S1](#)



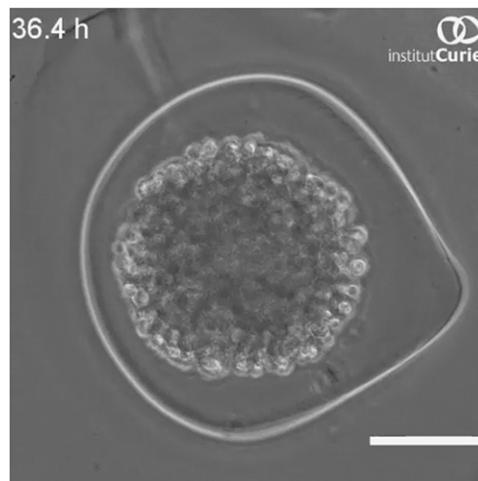
**Movie S2.** Growth of a CT26 spheroid inside an alginate gel capsule. Time-lapse, phase-contrast imaging shows the different phases of encapsulated spheroid growth. After confluence, the expanding spheroid deforms the capsule and a dark core is formed. Artificial coloring was added using After Effects. Images were recorded every 5 min. The video has been downscaled (high-resolution video is available on demand). (Scale bar:  $100 \mu\text{m}$ .)

[Movie S2](#)



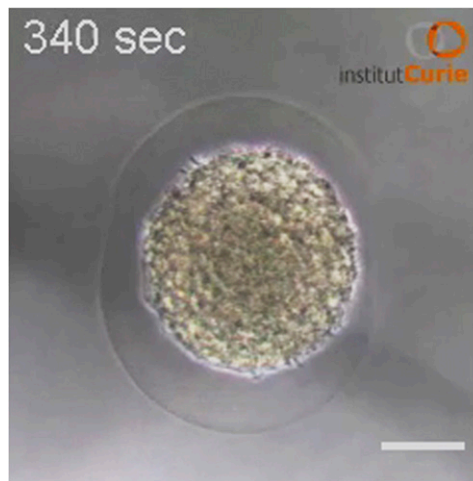
**Movie S3.** Bursting of a thin capsule after large deformation induced by spheroid growth. Time-lapse, phase-contrast imaging shows bursting of the alginate capsule and release of the cells, which spread onto an adhesive substrate. Images were recorded every 5 min. (Scale bar: 100  $\mu\text{m}$ .)

[Movie S3](#)



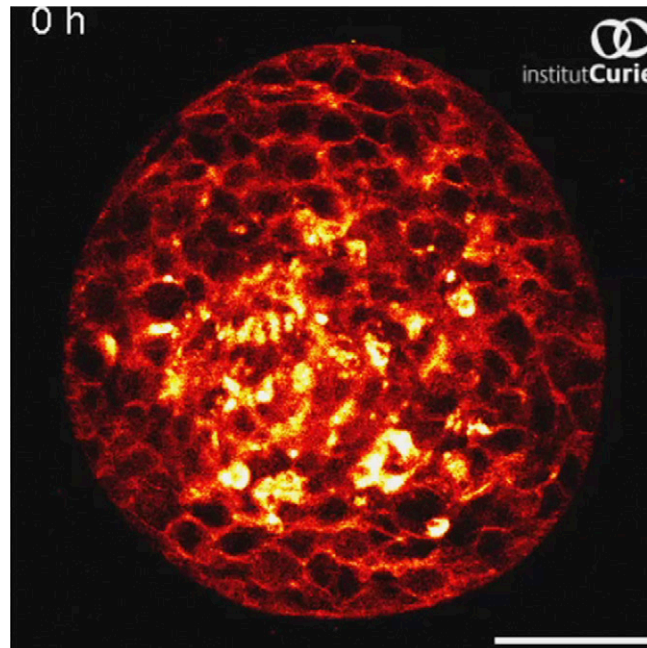
**Movie S4.** Growth of an S180 spheroid inside an alginate gel capsule. Time-lapse, phase-contrast imaging shows the spheroid reaching confluence. Images were recorded every 5 min. The video has been downsampled (high-resolution video is available on demand). (Scale bar: 100  $\mu\text{m}$ .)

[Movie S4](#)



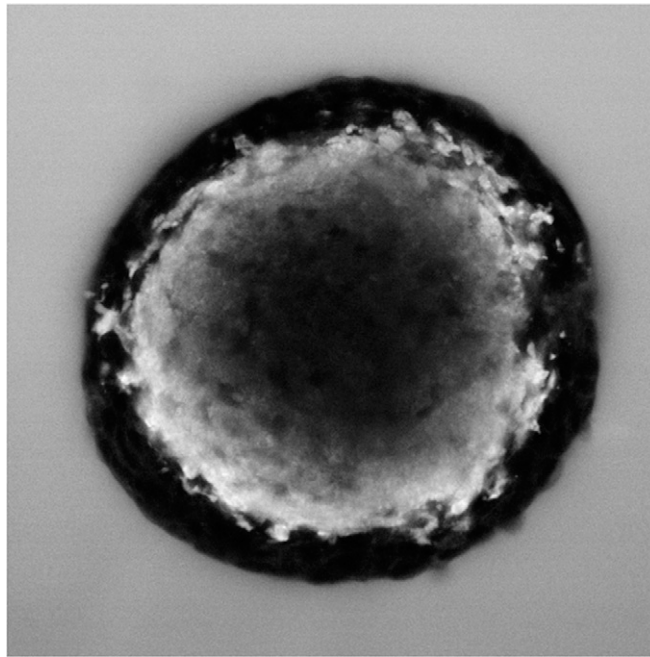
**Movie S5.** Recovery of bare spheroids by dissolution of the alginate shell. Time-lapse imaging shows the alginate capsule being dissolved in PBS. Images were recorded at a rate of one frame per second. (Scale bar: 100  $\mu\text{m}$ .)

[Movie S5](#)



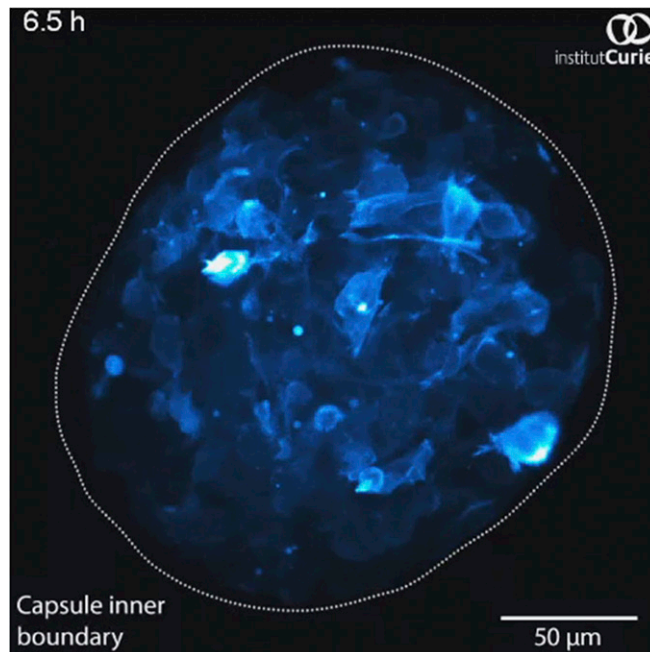
**Movie S6.** Growth of an encapsulated CT26 spheroid stained with FM4-64. Time-lapse confocal imaging (single plane extracted from 3D stack) shows the formation of an FM4-64-sensitive core after confluence. Images were recorded every 30 min. Excitation wavelength = 561 nm. A hot look-up table acquired using Fiji is shown (red). Images were processed by median filtering with kernel radius  $r = 1$  pixel. (Scale bar: 50  $\mu\text{m}$ .)

[Movie S6](#)



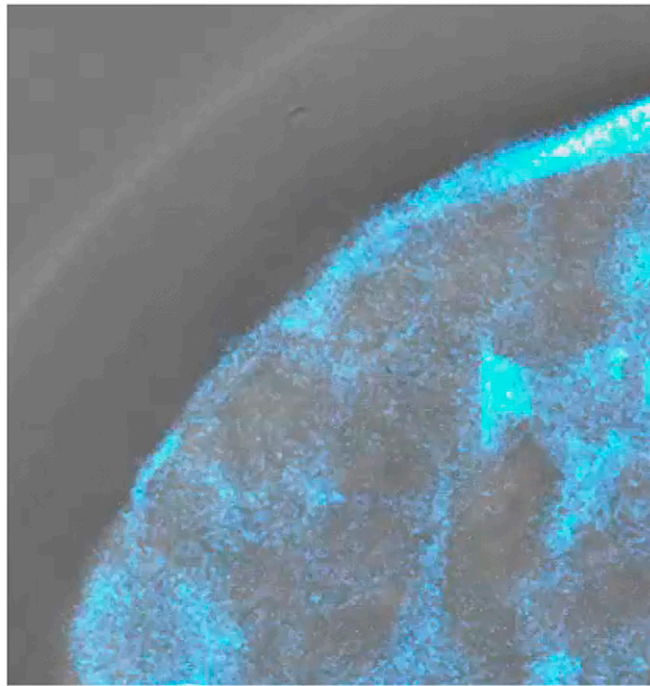
**Movie S7.** Core-shell structure of bare CT26 spheroids labeled with SRB after dissolution of the alginate shell in PBS. Time-lapse, two-photon imaging (single plane) is shown. The time interval between consecutive images is 1 min. Excitation wavelength = 830 nm. (Scale bar: 100  $\mu\text{m}$ .)

[Movie S7](#)



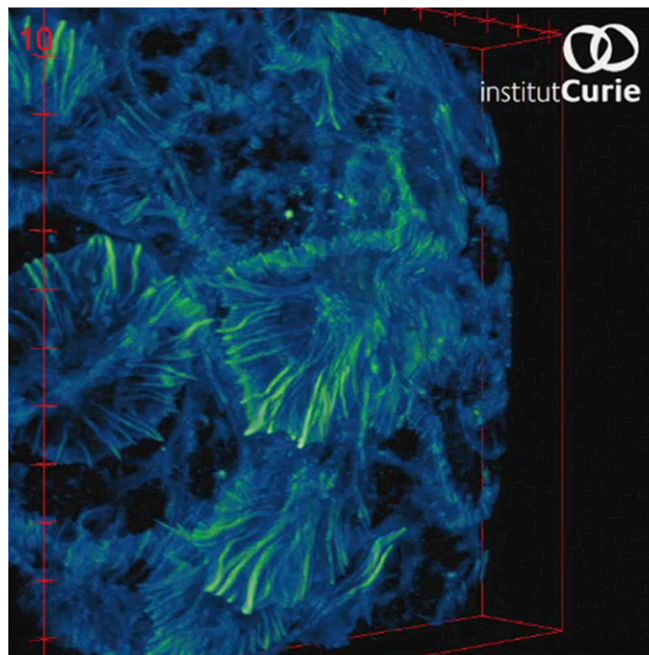
**Movie S8.** Growth of an encapsulated CT26-LifeAct-mCherry spheroid. Time-lapse confocal imaging (maximum intensity projection of 3D stack) shows the behavior of cells within the spheroid before and after confluence. Images were recorded every 15 min. Excitation wavelength = 561 nm. A hot look-up table acquired using Fiji is shown (cyan). Images were processed by median filtering with kernel radius  $r = 1$  pixel. The video has been downscaled (high-resolution video is available on demand). (Scale bar: 50  $\mu\text{m}$ .)

[Movie S8](#)



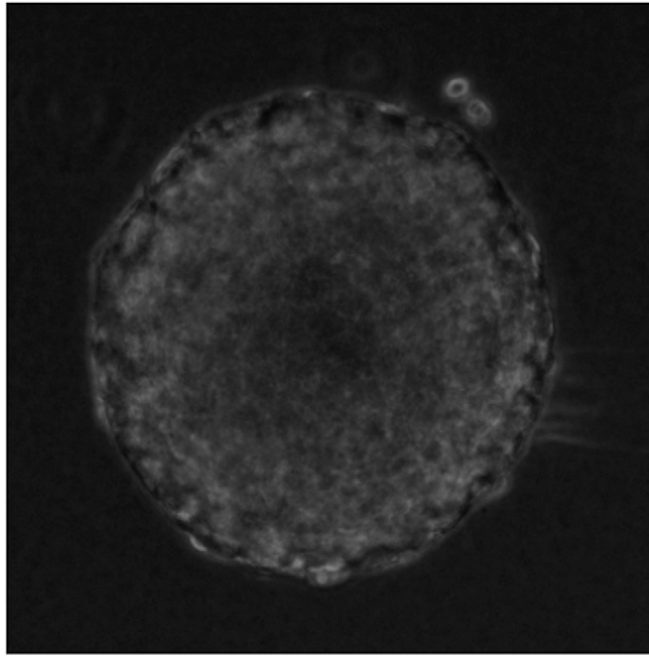
**Movie S9.** Growth of an encapsulated CT26-LifeAct-mCherry spheroid. An enlarged view of [Movie S8](#) shows cell migration parallel to the alginate border. (Scale bar: 10  $\mu\text{m}$ .)

[Movie S9](#)



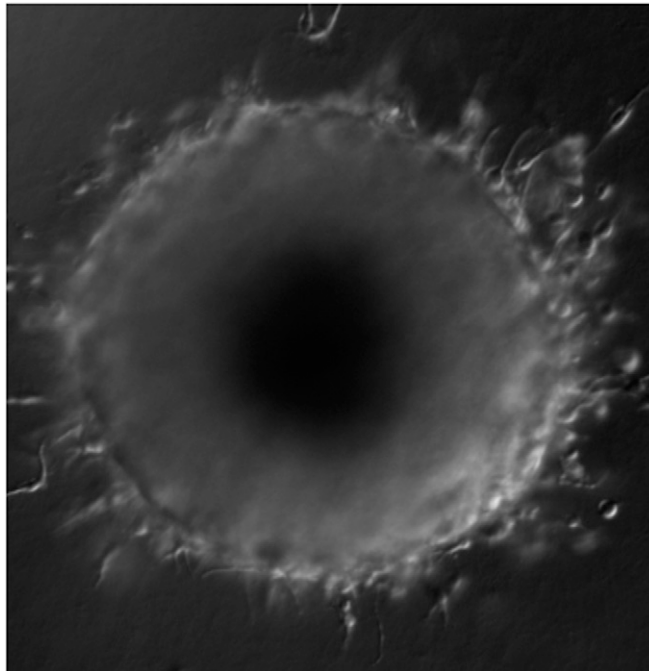
**Movie S10.** Surface of a fixed CT26 spheroid. The video shows the lamellipodia and filopodia structures revealed by phalloidin-Alexa488 staining. A 3D rendering of a stack encompassing a total volume of  $67.5 \times 67.5 \times 12.6 \mu\text{m}^3$  is shown; the original voxel size was  $0.066 \times 0.066 \times 0.14 \mu\text{m}^3$ . Excitation wavelength = 488 nm. A look-up table acquired using Fiji is shown (green fire blue). The video has been downscaled (high-resolution video is available on demand). The grid pitch is 5  $\mu\text{m}$ .

[Movie S10](#)



**Movie S11.** 3D motility assay of a freely grown CT26 spheroid embedded in collagen matrix. Time-lapse, phase-contrast imaging is shown. Images were recorded every 5 min. The video has been downscaled (high-resolution video is available on demand). (Scale bar: 100  $\mu\text{m}$ .)

[Movie S11](#)



**Movie S12.** 3D motility assay of a precompressed CT26 spheroid embedded in collagen matrix (after dissolution of the alginate shell). Time-lapse differential interference contrast imaging is shown. Images were recorded every 5 min. The video has been downscaled (high-resolution video is available on demand). (Scale bar: 100  $\mu\text{m}$ .)

[Movie S12](#)